ADVANCED ENERGY MATERIALS
www.advenergymat.de

Tailor-Made Buffer Materials: Advancing Uniformity and Stability in Perovskite Solar Cells

Thanh-Danh Nguyen, Doyeong Yeo, Ramesh Kumar Chitumalla, Sun-Ju Kim, Gyeong-Ho Jeong, Dong-Gun Kwun, Joonkyung Jang, In Hwan Jung,* and Ji-Youn Seo**

Along with the growing popularity of the p-i-n structure, bathocuproine (BCP) is increasingly recognized as a crucial buffer layer between the electron transport layer and electrode with the role of mitigating Schottky contact and enhancing performance. However, the chemical structure and role of its functional groups have not been thoroughly elucidated. This study introduces a novel modification of BCP in perovskite solar cells (PSCs) by altering functional groups to optimize their geometrical molecular structures and electronic properties. The substitution of aromatic phenyl and p-tolyl groups to 2,9-position on the BCP is highly effective in increasing the planarity of the conjugated backbone and protecting the reactive nitrogen atoms of the phenanthroline core, thereby improving charge transport and device stability. Experimental analyses, including electrostatic force microscopy, impedance spectroscopy, and photoluminescence, reveal that the modified BCP significantly enhances charge transport, reduces recombination losses, and markedly improves the structural stability of PSCs, leading to prolonged device lifetimes. The findings highlight the potential of structurally optimized BCP derivatives as a critical component in advancing high-efficiency and durable PSCs.

1. Introduction

Recently, perovskite solar cells (PSCs) have reported efficiencies exceeding 26% for single-junction devices, bringing them closer to commercialization, thanks to the efforts of many researchers. The most significant contributions have come from the development of techniques for forming high-crystallinity perovskite layers, advancements in electron and hole transport materials, and technologies that prevent electronic recombination at the interfaces.[1,2] The significance of interface contacts in PSCs can't be overstated, as they profoundly shape the overall performance and efficiency of the device. These interfaces, existing between different layers within the perovskite solar cell structure, exert a critical influence on charge carrier transport, recombination, and extraction – pivotal processes governing the transformation of sunlight into electricity. The perovskite layer, acting as the active layer, initiates the generation of electron-hole pairs. Subsequently, these charge carriers navigate through the electron transport layer (ETL) and the hole transport layer (HTL), ultimately migrating toward the electrode. However, the emergence of a Schottky barrier at the interface between the ETL and the electrode impedes the free movement of electrons,[3] necessitating the introduction of a buffer layer like Tris(8-hydroxyquinolinato) aluminum (Alq3),[4] Tin(IV) oxide (SnO_2),[5] and bathocuproine (BCP)[6] to mitigate this barrier. In which, BCP is gaining popularity in PSCs due to its ease of application through solution coating or thermal evaporation methods[7,8] and its ability to deliver high-performance. Thus, BCP is often used as a buffer layer between the ETL layer and the electrode, crucial for facilitating ohmic contact and reducing interfacial charge recombination.[3] Additionally, it acts as a barrier, preventing the inter-diffusion of harmful species into the perovskite absorber and inhibiting the egress of degradation products.[9]

However, despite the excellent electrical properties of BCP, its biggest drawback is that it easily reacts with moisture and oxygen, leading to reduced device long-term stability when exposed to air during the fabrication process or for use.[10,11] Research aimed at replacing high-performance BCP has been limited so far. Naphthalene diimide-based molecules were reported to replace the BCP buffer layer, but their highest power conversion efficiency (PCE) of 14.25% was much lower than the control BCP devices (15.57%).[12] The polymeric ETL containing BCP was also reported to enhance electron transport as well as hole-blocking properties in the p-i-n PSCs,[13] but it is only suitable for the solution process. The Blending of BCP and small molecules with a large dipole moment

T.-D. Nguyen, R. K. Chitumalla, S.-J. Kim, G.-H. Jeong, D.-G. Kwun, J. Jang, J.-Y. Seo
Department of Nano Fusion Technology
Pusan National University
Busan 46241, Republic of Korea
E-mail: jkjang@pusan.ac.kr; j-y.seo@pusan.ac.kr

D. Yeo, I. H. Jung
Department of Organic and Nano Engineering and Human-Tech Convergence Program
Hanyang University
222 Wangsimni-ro, Seongdong-gu, Seoul 04763, Republic of Korea
E-mail: inhjung@hanyang.ac.kr

The ORCID identification number(s) for the author(s) of this article can be found under https://doi.org/10.1002/aenm.202403633

DOI: 10.1002/aenm.202403633

significantly enhanced the V_{OC} of the PSCs,[14] but this study only focused on the additives to improve the performance of the BCP molecule.

In this study, we have developed new tailor-made buffer materials for the ETL that overcome the drawbacks of BCP while still maintaining or even enhancing its excellent electrical properties. Using density functional theory (DFT) calculations, we designed molecules that address the stereochemical limitations of conventional BCP and exhibit improved electrical characteristics. We repositioned the existing distorted phenyl group on BCP to a more optimal location that can protect the nitrogen of the pyridine while also making a more planar backbone structure. Our synthetic strategy was simple yet powerful, leading to encouraging results that surpassed the performance of existing BCP. Moreover, our novel BCP-m1 and BCP-m2 were synthesized through only one step while maintaining a similar molecular weight with BCP. It appears to be a very promising candidate as a vacuum deposition buffer layer. The newly developed BCP-m1 and BCP-m2 were coated on perovskite solar cells and perovskite/C60 layers using a vacuum deposition method. We observed the morphology using atomic force microscopy (AFM) and analyzed the electrical properties with electrostatic force microscopy (EFM). By fabricating p-i-n structured perovskite solar cells, we measured the efficiency and stability, confirming that the performance of the new materials is superior to that of conventional BCP.

2. Results and Discussion

2.1. Synthesis of Characterization of Novel Buffer Molecules

The design strategy for new buffer molecules, BCP-m1 and BCP-m2, focuses on optimizing the planarity and electronic interactions of these molecules to enhance their performance as buffer layers in PSCs. The parent molecule BCP has a non-planar structure, which has limitations in electronic coupling and strong interactions/adhesions with the adjacent layers. The BCP-m1 and BCP-m2 derivatives are engineered to exhibit increased planarity compared to BCP. By incorporating modifications that enhance the planarity of the molecular backbone, BCP-m1 and BCP-m2 improve their ability to form a more stable and continuous film. This increased planarity allows for better overlap with the C60 and perovskite layers, leading to more effective charge transport and reduced interfacial resistance. The chemical structure of BCP includes multiple aromatic rings, contributing to its stability and electronic properties. It has a phenanthroline core, a tricyclic aromatic compound consisting of three fused benzene rings, substituted with two methyl groups at positions 2 and 9, and two phenyl groups at positions 4 and 7. The methyl groups increase the solubility of BCP in organic solvents, facilitating solution-based fabrication techniques used in device manufacturing. The phenyl groups extend conjugation, provide steric protection, improve film formation, and modulate electronic properties.[15,16]

However, **Figure 1**d,g shows that the steric hindrance introduced by the methyl groups can limit the close packing of molecules, potentially reducing the efficiency of intermolecular interactions and charge transport. Under high thermal stress, methyl groups might also contribute to material degradation, a concern in environments where solar cells are exposed to high temperatures for prolonged periods. For these reasons, we replaced the methyl groups by moving the phenyl groups from positions 4 and 7 to positions 2 and 9, generating BCP-m1 (Figure 1b), and replaced the phenyl groups with p-tolyl groups, generating BCP-m2 (Figure 1c). The side view 3D structure of BCP-m1 and BCP-m2 in Figure 1h,i shows that these modifications significantly reduce steric hindrance, improving the close packing of molecules and thereby increasing the efficiency of intermolecular interactions and charge transport.

Herein, new BCP derivatives, BCP-m1 and BCP-m2, were designed and synthesized via a one-step Suzuki coupling reaction of commercially available 2,9-dichloro-1,10-phenanthroline with phenyl, and p-tolyl boronic esters, respectively. The synthesized BCP-m1 and BCP-m2 are highly soluble and air-stable, obtained as white crystalline solids with reaction yields of 50% and 85%, respectively. These newly synthesized BCP-m series were characterized through ^{1}H nuclear magnetic resonance (NMR) and ^{13}C NMR, with the spectra provided in Figures S1–S4 (Supporting Information) in the Supporting Information. Detailed synthetic routes of the BCP derivatives are shown in **Scheme 1**. Moreover, BCP-m1 and BCP-m2, with molecular weights of 332 and 360 g mol^{-1}, respectively, were designed to maintain a similar molecular weight to the parent BCP molecule (360 g mol^{-1}). Since the synthesized buffer molecules have molecular weights almost identical to the BCP, there is an advantage in being able to use the existing vacuum deposition process without significant modifications.

The absorption spectra of the BCP and synthesized BCP molecules were measured in both solution and film states. As shown in Figure S5a (Supporting Information), the maximum absorption peaks appeared at 282 nm for BCP, at 268 and 309 nm for BCP-m1, and at 275 and 316 nm for BCP-m2 in solution. Only BCP-m1 and BCP-m2 showed clear shoulder absorption, which strongly implies that BCP-m1 and BCP-m2 exhibit efficient π-conjugation between the BCP core and the phenyl and tolyl terminal units, respectively. In the comparison between BCP-m1 and BCP-m2, the absorption of BCP-m2 was slightly red-shifted compared to that of BCP-m1 because the p-tolyl group on BCP-m2 is more electron-donating than the phenyl group on BCP-m1, which enhances the π-conjugation with the electron-withdrawing BCP core. In the film state, control BCP exhibited a slight red-shift in absorption, but there was almost no change in the overall absorption. This indicates that there was no efficient π–π staking among the BCP molecules. On the contrary, the maximum absorption peaks were red-shifted to 272 and 314 nm for BCP-m1 and to 277 and 319 nm for BCP-m2. Additionally, the shoulder absorptions were more intense and broadened than those in the solution, indicating that the intermolecular interactions of BCP-m1 and BCP-m2 are highly enhanced in the film state. Detailed optical properties of the BCP and synthesized BCP molecules were summarized in Table S1 (Supporting Information).

For a better understanding of the molecular structure of the synthesized buffer molecules, the geometrical structure and electron density distribution of BCP, BCP-m1, and BCP-m2 were simulated by DFT calculations using the Gaussian 16 software package (see details in Supporting information). As shown in Figure 1, the phenyl ring on the control BCP was highly twisted from the BCP core unit. On the other hand, BCP-m1

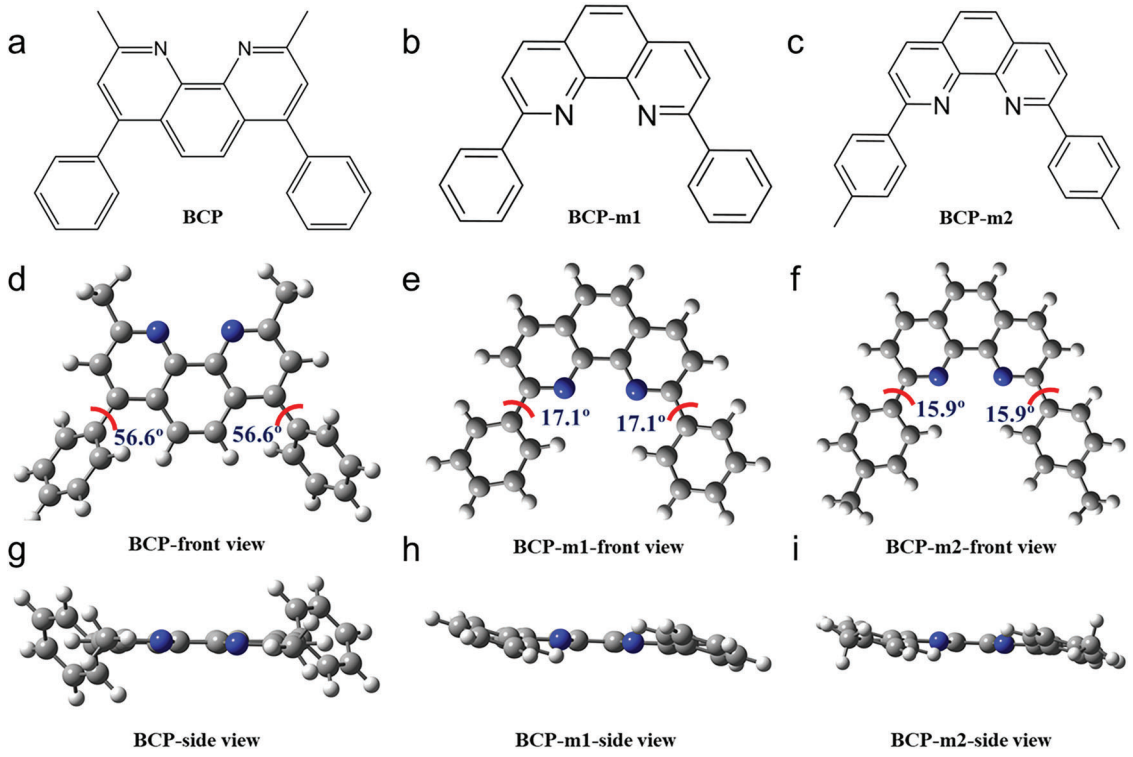

Figure 1. a–c) 2D chemical structures of BCP, BCP-m1, and BCP-m2. DFT-optimized 3D geometries, including d–f) front and g–i) side views, are shown to illustrate molecular conformations and dihedral angles. Hydrogen, carbon, and nitrogen atoms are represented by white, gray, and blue spheres, respectively.

and BCP-m2 exhibited quite a planar backbone structure. This strongly supported that BCP-m1 and BCP-m2 can have efficient π-conjugation and π–π intermolecular stacking, which is in good agreement with their absorption behavior. The increased planarity of BCP-m1 and BCP-m2 compared to BCP contributes to a more compact molecular structure, which can enhance stability. Moreover, while the nitrogen atoms on the control BCP are quite exposed to the air, the nitrogen atoms on BCP-m1 and BCP-m2 are significantly shielded by the bulky phenyl and tolyl groups, respectively. In the comparison between BCP-m1 and BCP-m2, it is observed that BCP-m2, which has tolyl groups, is in a more shielded environment. Consequently, BCP-m2 is expected to suppress the reactivity of phenanthroline most effectively, allowing for more stable operation within the device.

The optical bandgaps (E_g^{opt}) of the BCP and synthesized BCP molecules were calculated from the absorption onset wavelength of the film states, with BCP, BCP-m1, and BCP-m2 having values of 3.63, 3.30, and 3.23 eV, respectively. The highest occupied molecular orbital (HOMO) and lowest occupied molecular orbital (LUMO) energy levels of the BCP and synthesized BCP molecules were estimated through cyclic voltammetry (CV) with oxidation (E_{ox}) and reduction onset (E_{re}) potentials, as shown in Figure S5b (Supporting Information). The E_{ox} values of BCP, BCP-m1, and BCP-m2 were 1.79, 1.63, and 1.52 V, respectively, which correspond to HOMO energy levels (E_{HOMO}) of −6.14, −5.99 and −5.88 eV, respectively. The E_{re} values of BCP, BCP-m1, and BCP-m2 were −0.86, −0.82, and −0.81 V, and the corresponding LUMO energy levels (E_{LUMO}) were −3.49, −3.54 and −3.54 eV, respectively. The calculated electrochemical bandgap (E_g^{CV}) of BCP, BCP-m1, and BCP-m2 were 2.65, 2.45, and 2.34 eV, respectively. The bandgap of the buffer molecules was decreased in the order of BCP > BCP-m1 > BCP-m2, which is

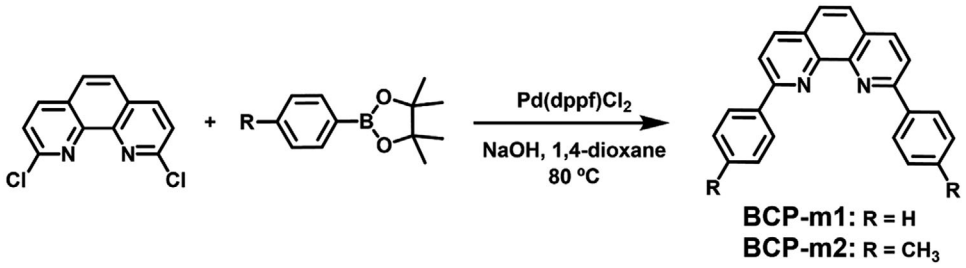

Scheme 1. Synthetic routes of BCP-m1 and BCP-m2.

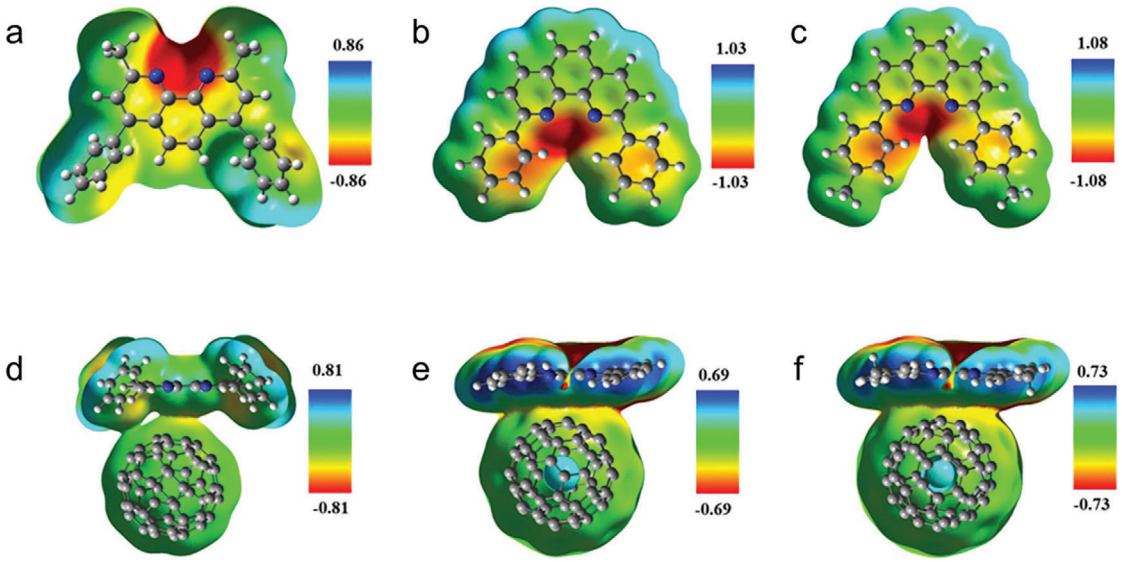

Figure 2. a–c) Simulated electrostatic potential maps of BCP, BCP-m1, and BCP-m2 and d–f) interactions between C60 and BCP, BCP-m1, and BCP-m2 are depicted in panels. Color-coded spheres represent hydrogen (white), carbon (gray), and nitrogen (blue) atoms. Electrostatic potential values, shown on a color scale, are provided in electron volts (eV).

consistent with the optical bandgap trend and suggests that BCP-m2 forms the most effective π-conjugation among the three buffer molecules. The simulated electrostatic potential (ESP) surfaces shown in **Figure 2**a–c exhibits a trend similar to the optical analysis outcomes. The enhanced π-electron delocalization within BCP-m1 and BCP-m2 is reflected in their ESP maps, suggesting improved potential for intermolecular interactions. This efficiently enhanced π-interaction capability and geometrically stable structure indicate that when deposited on C60, the newly designed molecules, BCP-m1 and BCP-m2, are energetically more stable than conventional BCP, as demonstrated in Figure 2d–f.

2.2. Morphology and Electrical Properties

To gain a deeper understanding of how modifying the functional groups within the BCP affects the overall performance of PSCs, several key properties were analyzed. To achieve this, we applied the newly synthesized BCP-m1 and BCP-m2 using the same deposition method as that used for conventional BCP, where BCP is deposited onto C60 using a thermal evaporator as demonstrated in Figure S8 (Supporting Information). As shown in the DFT calculation results in Figure S9 (Supporting Information), BCP-m1 and BCP-m2 are expected to form more structurally flat and stable bonds when deposited on C60, compared to conventional BCP. Initially, the surface morphology of the material was examined using scanning electron microscope (SEM) images, as shown in Figure S10 (Supporting Information). However, no significant differences were observed when comparing the SEM images of BCP, BCP-m1, and BCP-m2. AFM images in Figure S11 (Supporting Information) reveals differences in surface roughness among the samples. The BCP and BCP-m2 samples exhibit rougher surfaces compared to the BCP-m1 sample. By analyzing the line profiles extracted from the AFM images, these differences in roughness become more apparent: BCP shows the highest roughness with an average Ra of 12.268 nm, followed by BCP-m2 with Ra of 6.129 nm, and finally, BCP-m1 has the smoothest surface with Ra of 3.120 nm.

In addition, we employed EFM, a type of dynamic non-contact AFM, to examine the surface electrostatic forces of the materials.[17] The EFM images shown in **Figure 3**a,c,e, corresponding to BCP, BCP-m1, and BCP-m2, respectively, reveal

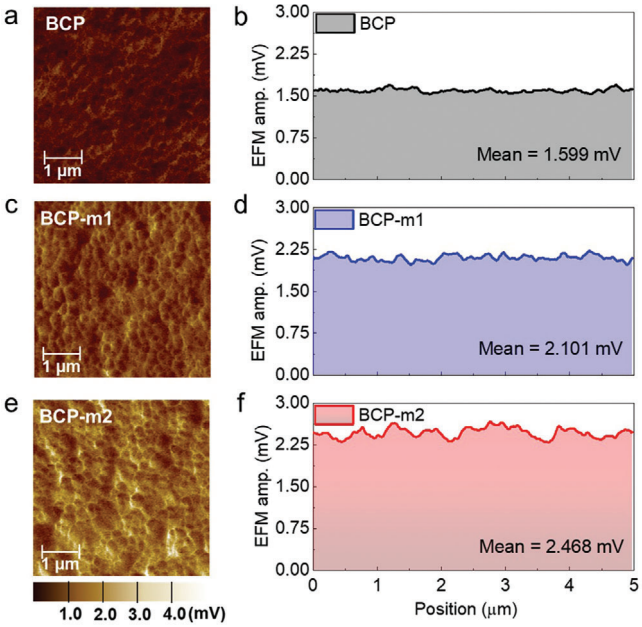

Figure 3. EFM surface electrostatic force images of a) BCP, c) BCP-m1, and (e) BCP-m2. The corresponding line profiles obtained from the EFM images of b) BCP, d) BCP-m1, and f) BCP-m2.

distinct differences in the electrostatic forces of the samples, highlighted by variations in color contrast. The EFM image for the BCP sample displays a dark brown color, indicating the lowest electrostatic force. In contrast, BCP-m1 exhibits a lighter brown color, suggesting a higher electrostatic force, while BCP-m2 shows a bright yellow color, representing the highest electrostatic force among the samples.

Similar to the AFM analysis, line profiles were extracted from the EFM images to further assess the differences in surface electrostatic forces across the materials. As shown in Figure 3b, the electrostatic force on the surface of BCP is relatively evenly distributed, with a mean value of 1.599 mV. However, the modified BCP samples (BCP-m1 in Figure 3d and BCP-m2 in Figure 3f exhibit less even distributions, with higher mean values of 2.101 and 2.468 mV, respectively. This difference can be attributed to the conductivity of the materials. During EFM measurement, a DC current is applied to both the material surface and the cantilever tip.[18] In materials with better conductivity, the interaction between the material and the cantilever tip is more pronounced, resulting in higher color contrast in the EFM image and an increased surface electrostatic force. Therefore, the higher color contrast and surface electrostatic force observed in the modified BCP samples indicate improved conductivity compared to the original BCP.

Surface electrostatic force plays a crucial role in charge conduction. As mentioned above, the surface electrostatic force of the modified BCPs is higher than that of the original BCP, suggesting that the modified BCPs may have enhanced charge separation capabilities compared to the original BCP. To validate this, we conducted (photoluminescence) PL measurements. The steady-state PL results in Figure S7a (Supporting Information) revealed a decrease in PL intensity when the BCP layer was replaced with BCP-m1 or BCP-m2. A lower PL intensity indicates reduced recombination of electron-hole pairs, signifying that a larger number of electrons were successfully extracted from the PVSK layer.[19] This observation supports our initial hypothesis that the charge extraction ability of the modified BCP layers is superior to that of the original BCP. To further elucidate the impact of molecular modifications on charge transport, we calculated the electron reorganization energies (EREs) for BCP, BCP-m1, and BCP-m2. As shown in Figure S15 (Supporting Information), the results indicate that BCP-m1 and BCP-m2 exhibit significantly lower EREs (0.256 and 0.245 eV, respectively) compared to BCP (0.425 eV). A lower ERE generally correlates with improved charge carrier mobility, suggesting that the structural modifications in BCP-m1 and BCP-m2 enhance their electron transport capabilities.

In addition, the carrier lifetime is another critical indicator of a material's charge extraction ability, so we conducted Time-Resolved Photoluminescence (TRPL) measurements. The TRPL results, presented in Figure S7b (Supporting Information), align with the steady-state PL findings. The BCP-m1 and BCP-m2 samples exhibited rapid photoluminescence decay compared to the BCP sample, which indicates efficient charge extraction rather than rapid recombination.[17] This superior charge extraction capability of the modified BCPs leads to reduced charge pair recombination, thereby contributing to the improved PCE of the device. This observation aligns with findings from prior studies, which show that faster TRPL decay is associated with enhanced charge extraction efficiency in perovskite-based devices.[20]

2.3. Comprehensive Device Characterization and Performance

In PSCs, resistance plays a significant role in determining the PCE of the device, making resistance testing essential. The results obtained from fitting the equivalent circuit reveal three typical resistances in PSCs.[21] The first is the series resistance (R_S), which represents the total resistive opposition that charge carriers (electrons and holes) face as they travel through the different layers of the solar cell.[22] Lower series resistance facilitates better charge transfer between the layers, leading to higher PCE. As shown in **Figure 4h**, the series resistance of the modified BCPs is lower than that of the original BCP. This finding aligns with the EFM results in Figure 3, indicating that the higher surface electrostatic force in the modified BCPs corresponds to better conductivity. The second resistance is the selective contact resistance (R_{SC}), which arises at the interfaces where charge carriers are collected selectively by the ETL and the HTL.[23] As depicted in Figure S13a (Supporting Information), there is no significant difference between the original BCP and the modified BCPs in terms of R_{SC}. This observation is consistent with the role of BCP as a buffer layer, which primarily conducts charges from the ETL to the electrode and thus has a minimal impact on charge collection. The recombination resistance is the final one. It refers to the resistance against the recombination of charge carriers (electrons and holes) within the solar cell, higher recombination resistance indicates a lower rate of recombination, which is desirable for achieving high PCE in solar cells.[24] Figure S13b (Supporting Information) shows that BCP-m2 exhibits the highest recombination resistance among the samples, which correlates with the PL and TRPL results in Figure S7 (Supporting Information), this indicates that BCP-m2 has a strong potential to suppress electron recombination, thereby improving the PCE of the device.

To confirm the above inferences, we fabricated a device with a simple structure ITO/MeO-4PACz/Triple cation perovskite/C60/BCP or BCP-m/Ag, as shown in Figure 4a. Using cyclic voltammetry calculations (Figure S5b, Supporting Information), we constructed the band alignment schematic shown in Figure 4b. A slight change in the bandgap is observed when BCP is modified, the bandgap of both BCP-m1 and BCP-m2 are smaller than BCP and the smallest bandgap is BCP-m2 with the same HOMO level. This reduction brings the LUMO level of BCP-m1 and BCP-m2 closer to the LUMO of C60, which positively influences electron injection from C60 to the Ag electrode. To better understand the effect of BCP modification on the band diagram, Ultraviolet Photoelectron Spectroscopy (UPS) analysis was performed, as shown in Figure S6a–d (Supporting Information). The results reveal an increase in the work function and a corresponding shift in the valence band level across the series of BCP, BCP-m1, and BCP-m2. When combined with the electrochemical bandgap data from CV (Figure S5b, Supporting Information), the UPS analysis indicates a downward shift in conduction band energy from BCP to BCP-m1 and BCP-m2, as depicted in Figure 4c. Furthermore, as shown in Figure 4b, the reduction in conduction band energy aligns the modified BCP samples, particularly BCP-m2, more closely with the perovskite

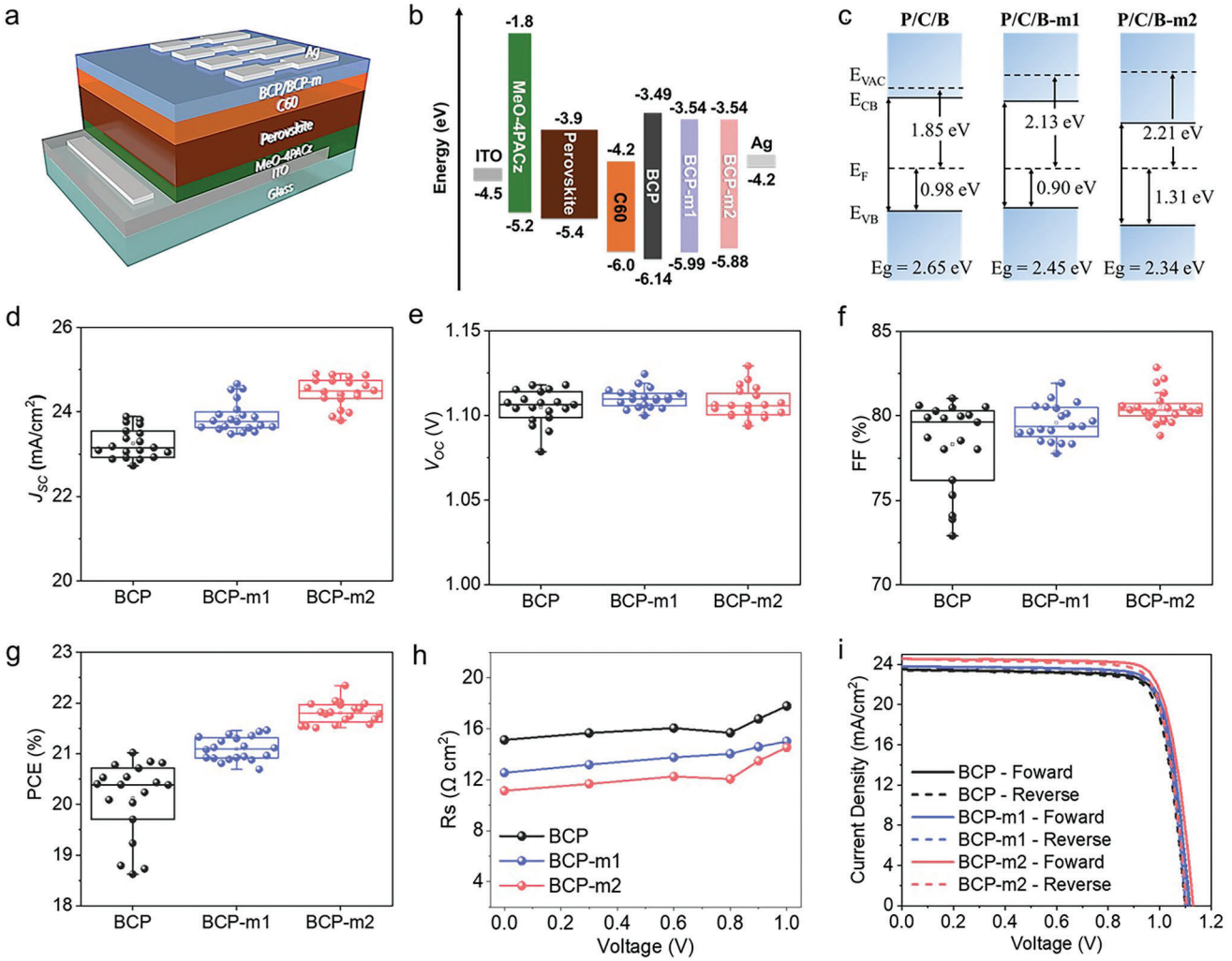

Figure 4. a) Schematic structure of the perovskite solar cell, b) Schematic illustration of bandgap alignment of BCPs. c) Schematic band diagram of BCP, BCP-m1, and BCP-m2. Box chart illustrating the statistical distribution of d) Current Density (J_{SC}), e) Open-Circuit Voltage (V_{OC}), f) Fill Factor (FF), g) Power Conversion Efficiency (PCE) under simulated AM1.5G sunlight. Impedance spectroscopy of PSCs with BCP, BCP-m1, and BCP-m2: h) series resistance. i) *J–V* curves were obtained from reverse scans (solid) and forward scans (dash) for perovskite solar cells under different conditions.

conduction band, thereby enhancing electron injection efficiency. The improvement in PCE when using the modified BCPs is readily apparent. Specifically, the PCE of these solar cells, measured under standard AM 1.5G solar conditions, shows a notable enhancement with the modified BCP samples. As shown in Figure 4d–g and detailed in **Table 1**, the BCP-m2 sample significantly improves all key parameters—V_{OC} (open-circuit voltage), J_{SC} (short-circuit current density), FF (fill factor) and PCE compared to the original BCP sample. The average PCE increases from 20.02%, with a maximum efficiency of 21.01% for BCP, to 22.34% with a maximum efficiency of 21.81% for BCP-m2. While BCP-m1 also shows a slight improvement in efficiency compared to BCP, it remains lower than that achieved with BCP-m2. The band alignment between material layers in PSCs plays a crucial role in understanding carrier conduction and separation.

For hysteresis analysis, the *J–V* curve was scanned in both forward and reverse directions. As shown in Figure 4i and **Table 2**, the results indicate a clear improvement in hysteresis for the modified BCP samples compared to the original BCP. The forward and reverse *J–V* curves for the modified BCPs show minimal variation, suggesting that these modifications effectively reduce ion migration within the device. This reduced hysteresis is a positive indicator of the stability and performance

Table 1. Photovoltaic parameters corresponding to the box chart as shown in Figure 4d–g.

Sample		J_{SC}[mA cm^{-2}]	V_{OC}[V]	FF[%]	PCE[%]
BCP	Maximum	23.54	1.11	80.04	21.01
	Average	23.25	1.10	78.31	20.02
BCP-m1	Maximum	23.78	1.11	81.06	21.46
	Average	23.88	1.11	79.58	21.10
BCP-m2	Maximum	24.56	1.12	80.53	22.34
	Average	24.47	1.11	80.52	21.81

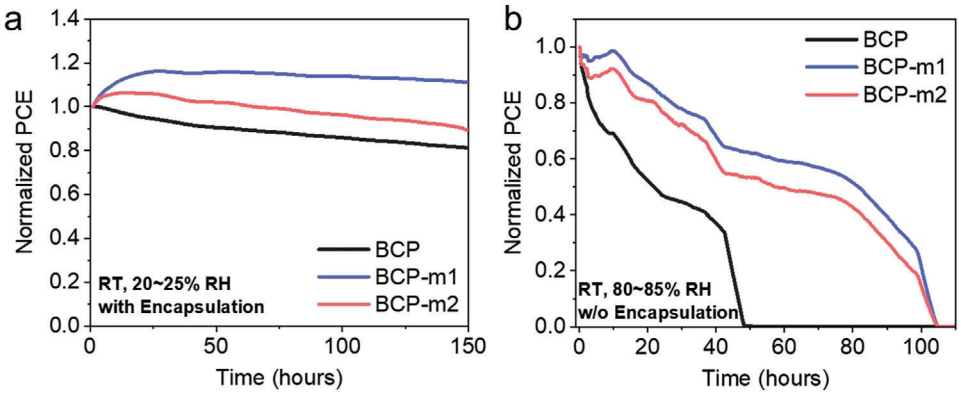

Figure 5. MPPT test of perovskite solar cell under light soaking (AM 1.5 G, 100 Mw cm^{-2}): a) in 20–25% humidity at room-temperature with encapsulation, and b) in 80–85% humidity condition at room-temperature without encapsulation.

consistency of the PSCs with modified BCP layers. The incident photon-to-electron conversion efficiency (IPCE) was analyzed to gain further insight into the photon-to-electron conversion efficiency across the wavelength range of 300–850 nm. As shown in Figure S14 (Supporting Information), both BCP-m1 and BCP-m2 exhibit improved photon-to-electron conversion efficiency compared to the original BCP, with BCP-m2 demonstrating the highest efficiency. Given that current density is integrated from the IPCE, a clear correlation emerges: higher photon-to-electron conversion efficiency directly leads to higher current density, and conversely, lower efficiency results in lower current density. To investigate the impact of the chemically stable structure, where the reactive nitrogen atoms are positioned inside the BCP-m molecules, on long-term stability in PSC devices, we established two different evaluation conditions. First, to isolate the effect of structural differences on long-term stability, we encapsulated the devices to prevent interactions between the buffer molecules and water. Additionally, to assess whether the molecules designed for moisture resistance retain stability under operational conditions, we tracked the maximum power point tracking (MPPT) without encapsulation in 80–85% relative humidity. As shown in **Figure** 5a, encapsulated BCP-m1 and BCP-m2 samples demonstrated better long-term stability compared to the BCP sample. After 150 h of measurement, the BCP sample exhibited the most significant reduction in PCE, dropping to ≈80%, while the PCE of BCP-m1 and BCP-m2 remained above 90%, with BCP-m1 showing the highest stability. To further understand the impact of environmental factors on device performance, we conducted a long-term stability test under high humidity (80-85% RH) using a standard AM 1.5G light source, as shown in Figure S16 (Supporting Information). The results, presented in Figure 5b, reveal a clear performance degradation in the original BCP sample compared to BCP-m1 and BCP-m2. While the BCP sample lasted less than 50 h under high humidity, both BCP-m1 and BCP-m2 endured for over 100 h—double the lifespan of the BCP sample. These long-term stability test results confirm that the structurally stable, tailor-made BCP-m molecules effectively enhance the long-term stability of solar cells in high-humidity environments by providing protection against moisture.

Table 2. Photovoltaic parameters corresponding to the *J–V* curves hysteresis as shown in Figure 4i.

Sample		J_{SC}[mA cm^{-2}]	V_{OC}[V]	FF[%]	PCE[%]
BCP	Forward	23.54	1.11	80.04	21.01
	Reverse	23.45	1.09	79.84	20.60
BCP-m1	Forward	23.78	1.11	81.06	21.46
	Reverse	23.82	1.10	80.54	21.10
BCP-m2	Forward	24.56	1.12	80.53	22.34
	Reverse	24.50	1.10	79.91	21.62

3. Conclusion

This study demonstrates that strategic modification of the functional groups of the BCP buffer layer can significantly enhance the PCE and durability of solar cells. By simply replacing the methyl groups at the 2,9-positions of BCP with aromatic phenyl and p-tolyl groups, significant enhancement in the backbone planarity and π-conjugation was achieved. Notably, the p-tolyl groups on the newly synthesized BCP-m2 most effectively shielded the reactive nitrogen atoms of the phenanthroline core while maintaining a planar backbone structure. This was highly beneficial for enhancing charge transport and improving the device stability of PSCs. Through complementary analyses, including simulated EREs from DFT calculations, microscopic spectroscopy, and photovoltaic characterization, it was shown that the modified BCP samples offer improved charge transfer compared to the original BCP, leading to enhanced device performance. Additionally, these modifications contribute to greater device stability, reduced hysteresis, and improved long-term stability. This study provides valuable insights into the evaluation and modification of functional groups in materials to achieve more optimal results in both the performance and stability of solar cells.

Supporting Information

Supporting Information is available from the Wiley Online Library or from the author.

Acknowledgements

T-D.T., D.Y., R.K.C., and S-J.K. contributed equally to this work. J-Y.S. is grateful to the Ministry of Trade, Industry and Energy (MOTIE) and Korea Institute for Advancement of Technology (KIAT) through the International Cooperative R&D program (P0026100) and National Research Foundation of Korea(NRF) grant funded by the Korea government(MSIT) (RS-2024-00406152). J.J. acknowledges the support by the National Research Foundation of Korea(NRF) grant funded by the Korea government(MSIT) (RS-2023-00220748). This work was supported by the Technology Innovation Program (RS-2024-00422305, Development of deposition-type highly heat-resistant Near-infrared emitting/absorbing organic materials and device for implementation of all-in one sensor OLED display) funded by the Ministry of Trade, Industry and Energy (MOTIE, Korea).

Conflict of Interest

The authors declare no conflict of interest.

Data Availability Statement

The data that support the findings of this study are available from the corresponding author upon reasonable request.

Keywords

buffer layer, modified bathocuproine, perovskite solar cells, stability, thermal evaporation

Received: August 14, 2024
Revised: September 30, 2024
Published online: November 13, 2024

[1] Y. Chen, J. Hu, Z. Xu, Z. Jiang, S. Chen, B. Xu, X. Xiao, X. Liu, K. Forberich, C. J. Brabec, Y. Mai, F. Guo, *Adv. Funct. Mater.* **2022**, *32*, 19.
[2] J. Warby, F. Zu, S. Zeiske, E. Gutierrez-Partida, L. Frohloff, S. Kahmann, K. Frohna, E. Mosconi, E. Radicchi, F. Lang, S. Shah, F. Peña-Camargo, H. Hempel, T. Unold, N. Koch, A. Armin, F. De Angelis, S. D. Stranks, D. Neher, M. Stolterfoht, *Adv. Energy Mater.* **2022**, *12*, 2103567.
[3] N. Yadav, P. Roy, A. Khare, *Mater. Sci. Eng. B.* **2023**, *293*, 116458.
[4] L. Chen, G. Wang, L. Niu, Y. Yao, Y. Guan, Y. Cui, Q. Song, *RSC Adv.* **2018**, *8*, 15961.
[5] J. Kern, J. Heitmann, M. Müller, *ACS Appl. Energy Mater.* **2023**, *6*, 2199.
[6] C. Chen, S. Zhang, S. Wu, W. Zhang, H. Zhu, Z. Xiong, Y. Zhang, W. Chen, *RSC Adv.* **2017**, *7*, 35819.
[7] Q. B. Ke, J. R. Wu, S. E. Chiang, C. C. Cheng, Y. W. Su, I. J. Hsu, J. M. Yeh, S. H. Chang, *Sol. Energy Mater. Sol. Cells* **2022**, *242*, 111782.
[8] N. Shibayama, H. Kanda, T. W. Kim, H. Segawa, S. Ito, *APL Mater.* **2019**, *7*, 3.
[9] P. Chen, Y. Xiao, J. Hu, S. Li, D. Luo, R. Su, P. Caprioglio, P. Kaienburg, X. Jia, N. Chen, J. Wu, Y. Sui, P. Tang, H. Yan, T. Huang, M. Yu, Q. Li, L. Zhao, C. H. Hou, Y. W. You, J. J. Shyue, D. Wang, X. Li, Q. Zhao, Q. Gong, Z. H. Lu, H. J. Snaith, R. Zhu, *Nature* **2024**, *625*, 516.
[10] G. Z. Liu, C. S. Du, J. Y. Wu, B. T. Liu, T. M. Wu, C. F. Huang, R. H. Lee, *Polhin* **2020**, *13*, 42.
[11] Z. Zheng, Z. Xue, K. Zhao, Y. Yang, X. Zhu, H. Li, S. Cheng, S. Li, N. Yan, Z. Wang, *Sol. RRL* **2024**, *8*, 2301076.
[12] S. Valero, A. Cabrera-Espinoza, S. Collavini, J. Pascual, N. Marinova, I. Kosta, J. L. Delgado, *Eur. J. Org. Chem.* **2020**, *2020*, 5329.
[13] F. F. Wang, T. X. Liu, Z. W. Cui, L. Y. Wang, Y. J. Dou, X. Y. Shi, S. W. Luo, X. D. Hu, Z. J. Ren, Y. Y. Liu, Y. Zhao, S. S. Chen, *Chin. J. Polym. Sci.* **2024**, *42*, 1060.
[14] P. Fassl, S. Ternes, V. Lami, Y. Zakharko, D. Heimfarth, P. E. Hopkinson, F. Paulus, A. D. Taylor, J. Zaumseil, Y. Vaynzof, *ACS Appl. Mater. Interfaces* **2019**, *11*, 2490.
[15] T. Saito, *Sep. Sci. Technol.* **1994**, *29*, 1335.
[16] H. Gao, C. Qin, H. Zhang, S. Wu, Z. M. Su, Y. Wang, *J. Phys. Chem. A* **2008**, *112*, 9097.
[17] Y. Wu, W. Chen, Z. Wan, A. B. Djurišić, X. Feng, L. Liu, G. Chen, R. Liu, Z. He, *J. Power Sources* **2019**, *425*, 130.
[18] A. Gomez, Q. Wang, A. R. Goni, M. Campoy-Quiles, A. Abate, *Energy Environ. Sci* **2019**, *12*, 2537.
[19] M. Liu, S. Dahlström, C. Ahläng, S. Wilken, A. Degterev, A. Matuhina, M. Hadadian, M. Markkanen, K. Aitola, A. Kamppinen, J. Deska, O. Mangs, M. Nyman, P. D. Lund, J. H. Smått, R. Österbacka, P. Vivo, *J. Mater.Chem. A* **2022**, *10*, 11721.
[20] S. De Wolf, J. Holovsky, S. J. Moon, P. Loper, B. Niesen, M. Ledinsky, F. J. Haug, J. H. Yum, C. Ballif, *J .Phys. Chem. Lett.* **2014**, *5*, 1035.
[21] Y. Jiang, E. J. Juarez-Perez, Q. Ge, S. Wang, M. R. Leyden, L. K. Ono, S. R. Raga, J. Hu, Y. Qi, *Mater. Horiz.* **2016**, *3*, 548.
[22] D. Pysch, A. Mette, S. W. Glunz, *Sol. Energy Mater. Sol. Cells* **2007**, *91*, 1698.
[23] U. Rau, T. Kirchartz, *Adv. Mater. Interfaces* **2019**, *6*, 20.
[24] L. Duan, H. Yi, C. Xu, M. B. Upama, M. A. Mahmud, D. Wang, F. H. Shabab, A. Uddin, *IEEE J. Photovoltaics* **2018**, *8*, 1701.

